ELSEVIER

Physics of the Earth and Planetary Interiors 133 (2002) 159–179

PHYSICS OF THE EARTH AND PLANETARY INTERIORS

www.elsevier.com/locate/pepi

Paleointensity measurements of pyroclastic flow deposits co-born with widespread tephras in Kyushu Island, Japan

Aska Takai [a], Hidetoshi Shibuya [b], Arata Yoshihara [a,*], Yozo Hamano [a]

[a] *Department of Earth and Planetary Science, Graduate School of Science, University of Tokyo, Tokyo 113-0033, Japan*
[b] *Department of Earth Sciences, Faculty of Science, Kumamoto University, Kumamoto 860-8555, Japan*

Received 2 February 2002; received in revised form 30 April 2002; accepted 1 July 2002

Abstract

We report the results of paleointensity determination with welded pyroclastic flow deposits co-born with widespread tephras derived from Kikai (K-Ah, 7.3 ka), Aira (AT, 28 ka), and Aso (Aso-1, 270 ka; Aso-2, 140 ka; Aso-3, 120 ka; Aso-4, 90 ka) calderas in Kyushu Island, Japan. Since the widespread tephras are commonly used as good key layers, their ages and oxygen isotope stages have been well established. Thermal demagnetization and several rock magnetic experiments showed that the pyroclastic flow samples had stable remanent magnetizations and are suitable for paleointensity measurements. Using Thelliers' method, we obtained reliable paleointensities from six eruptive units, and calculated corresponding virtual dipole moment (VDM) values ranging from 2.7 to 9.7 $\times$ 10^{22} A m^2. VDMs for the youngest units, K-Ah and AT, are consistent with the global trend of increasing dipole moment for the past 40 kyr. Aso-4, -3 and -1 yield moderate VDMs similar to the mean paleointensity for the past 1 Myr, and especially, the results from Aso-4 and -3 show good agreement with the VDM variation between 70 and 130 ka obtained from La Réunion Island [J. Geophys. Res. 96 (1991) 1981; Earth Planet. Sci. Lett. 140 (1996) 173]. A low VDM value and an abnormal VGP position obtained from Aso-2 suggest a possibility that Aso-2 records an excursion-like event occurred around 140 ka between Blake and Jamaica events.

Keywords: Paleointensity; Pyroclastic flow; Tephra; Sint-800; Sedimentary core

1. Introduction

Geomagnetic secular variation studies have been long focused mainly on fluctuations in the field directions or on the corresponding pole positions. However, the secular variation of the geomagnetic field intensity is also important as well as the paleodirectional works, in order to understand the dynamics of the core powering the geodynamo.

Paleointensity studies with the records from sedimentary cores have been recently developed. Sediments are the only material which may record the behavior of the past geomagnetic field continuously. In addition, it is generally believed that the intensity variations recorded in sediments are derived from the changes in the dipole moment because of the time-averaged nature of sedimentary magnetizations. However, the complicated nature of detrital remanent magnetization (DRM) prohibits us to estimate the absolute value of the field intensity from the sedimentary record. Thus, there have been some efforts to construct the reference paleointensity secular variation curve by combining the sedimentary records and the paleointensity studies on volcanic rocks. For example, Guyodo and Valet (1999) determined the

* Corresponding author. Fax: +81-3-5841-8791.
E-mail address: yosihara@sys.eps.s.u-tokyo. ac.jp (A. Yoshihara).

0031-9201/02/$ – see front matter
PII: S0031-9201(02)00090-0

absolute value of Sint-800, which is their composite intensity curve for the past 800 kyr, by fitting with the absolute paleointensity data obtained from volcanic rocks for the past 40 kyr. The trend of variation in Sint-800 is consistent with volcanic data and many sedimentary core data for this period. However, the reliability for the older period seems debatable, and it is necessary to be cross-checked with absolute paleointensity values during the earlier period.

Volcanic records, on the other hand, have the great advantage for the paleointensity studies. Their magnetization processes are relatively well understood, and can be reliably reproduced in the laboratory, thus, we can evaluate the absolute values of paleointensity reasonably. Moreover, the volcanic records do not suffer from possible environmental factors and from the time-averaging effect inherent in the sedimentary acquisition of the remanence. Therefore, volcanic records can provide better quantitative appraisals of the past geomagnetic field intensities, despite their discontinuity.

In the present study, paleointensities were determined with the pyroclastic flow deposits co-born with widespread tephras derived from Kikai, Aira, and Aso calderas in Kyushu Island, Japan. Since dense-welded pyroclastic flow deposits are considered to possess thermoremanent magnetization (TRM), they are available for absolute paleointensity determinations by Thelliers' method (Thellier and Thellier, 1959). Their principal advantage is that the stratigraphic positions of the simultaneous widespread tephras have been well established in the oxygen isotopic stratigraphy, in addition to the ages by a variety of isotope dating methods, the mineralogy, and the distributions, since they are commonly used as good key layers over a wide area including the ocean bottom sediments. Therefore, paleointensity determinations from these pyroclastic flows, combined with the information about the tephras and their oxygen isotope stages, will be able to be compared precisely with relative intensity curves obtained from sedimentary cores. Unfortunately, no relative paleointensity record including these tephras has been reported to the present, and few records have provided the oxygen isotope data with sufficient resolution to distinguish the sub-stages. However, when cores of magnetically uniform sediments except for including these tephras are discovered, or cores which are correlated with oxygen isotope stages to the detail are reported, the absolute values obtained from the pyroclastic flows would be able to provide the calibration points of virtually error free in the age for the relative intensity curve. Aside from a possibility of calibration of sedimentary records, the paleointensity determinations with these pyroclastic flows have large significance in that their ages are strictly tied to the oxygen isotope stages, being essentially different from other absolute data.

2. Geology and sampling

Kyushu Island is located in the southwest of Japan (Fig. 1). In Kyushu Island, there are four large calderas (Aso, Aira, Ata, and Kikai calderas) with diameters of about 20 km along the volcanic front originated from the subduction of the Philippine Sea plate. These calderas are considered to have been formed during the middle to late Pleistocene time, by several explosive eruptions accompanied with widespread tephras and pyroclastic flows. The targets of the present study are the dense-welded pyroclastic flow deposits co-born with widespread tephras of Aso, Aira, and Kikai calderas (Fig. 1). Welded pyroclastic flow deposits of these calderas are widely distributed in Kyushu Island, and generally well suited for paleomagnetic researches.

Aso volcano is one of the largest calderas in the world and covers an area of 380 km^2. It is well known that the pyroclastic flow deposits are divided into four major eruptive units which have occurred between 90 and 270 ka. They were accompanied by four sets of the pyroclastic flow and widespread tephra referred to as Aso-1, -2, -3, and -4 in ascending order. Furthermore, Aso-2, -3, and -4 are divided into two (Aso-2A and -2B), three (Aso-3A, -3B, and -3C), and two subunits (Aso-4A and -4B), respectively (Ono et al., 1977). The samples were collected at 13 sites from five subunits (Aso-l, -2A, -2B, -3B, -4A, and -4B) of four eruptive units. At Aira and Kikai calderas, we collected Ito pyroclastic flow deposits co-born with Aira-Tn (AT) tephra with an age of 29 ka (Okuno, 2001; Shirai, 2001), and Funakura pyroclastic flow deposits co-born with Kikai-Akahoya (K-Ah) tephra with an age of 7.3 ka (Okuno, 2001; Shirai, 2001), respectively. These widespread tephras are thought to have spread over distances of at least 1300 km. In this

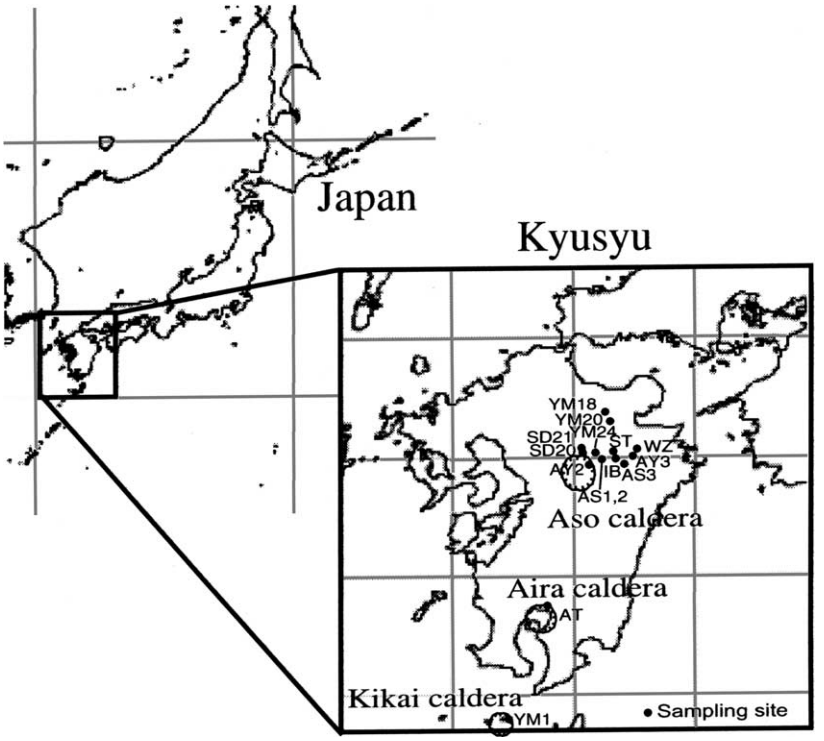

Fig. 1. Map of Kyusyu Island, showing the calderas and the sampling sites (solid circles).

paper, for convenience of description, we use the abbreviation of the widespread tephra (i.e. K-Ah, AT, Aso-1, -2, -3 and -4) as a name for each eruptive unit (set of pyroclastic flow and widespread tephra).

The lithology of Aso-1 is represented by pyroxene rhyolite, and that of Aso-2 and -3 is represented by pyroxene rhyolite and andesite. Aso-4 is characterized by pyroxene-homblende rhyolite and dacite (Ono et al., 1977). For AT and K-Ah, pyroxene rhyolite and pyroxene dacite are representative, respectively. The eruptive age for each widespread tephra has been well investigated by several previous studies using a variety of dating methods. Moreover, because these tephras are distributed over a wide area including the bottom of the sea, oxygen isotope stages corresponding to these tephras were also generally well known. The most recent reliable ages are summarized in Table 1.

Table 1
Results of age determination recently reported

Tephra name	Dating method	Age (ka)	$\delta^{18}O$ stage	Reference
K-Ah	^{14}C	7.3	1	Okuno (2001)
A-Tn	^{14}C	29	3a (29 ka)	Okuno (2001), Shirai (2001)
Aso-4	K-Ar	89 ± 7	5b (88 ka)	Matsumoto et al. (1991), Shirai (2001)
Aso-3	K-Ar	123 ± 6	5e (122 ka)	Matsumoto et al. (1991), Yoshikawa and Kuwae (2001)
Aso-2	K-Ar	141 ± 5		Matsumoto et al. (1991)
Aso-1	K-Ar	266 ± 14	8b (255 ka)	Matsumoto et al. (1991), Shirai (2001)

^{14}C ages are after atmospheric radiocarbon calibration (Kitagawa and Plicht, 1998). Oxygen isotope stages are also represented.

Table 2
List of the sampling localities of dense welded pyroclastic flow deposits co-born with widespread tephras

Unit	Site	Longitude (E)	Latitude (N)
K-Ah (Funakura flow)	YM1	130°25′10″	30°48′42″
AT (Ito flow)	AT	130°47′39″	31°46′41″
Aso-4B	IB	131°16′41″	33°57′57″
	ST	131°17′52″	32°56′36″
Aso-4A	YM20	131°16′48″	33°14′58.4″
	YM24	131°12′50″	33°9′2″
	YM18	131°17′25″	33°25″
	WZ	131°271′5″	32°57′41″
Aso-3B	AS3	131°21′34″	32°54′09″
	AY3	131°24′40″	32°55′36″
Aso-2B	AY2	131°08′50″	32°56′35″
	SD21	131°08′03″	32°59′38″
Aso-2A	AS2	131°12′08″	32°59′55″
	SD20	131°07′53″	32°59′28″
Aso-1	AS1	131°13′32″	32°59′32.5″

We sampled the dense-welded pyroclastic flow deposits of the above mentioned six eruptive units derived from three calderas. The details of the sampling localities are given in Table 2. In each sampling site, 6–17 samples oriented by a magnetic compass were collected. At site AS1 (Aso-1), grayish and reddish colored rocks were observed, and both types of the samples were collected.

3. Paleomagnetic directions

To separate characteristic remanent magnetization (ChRM) components of the samples, we carried out thermal demagnetization (ThD) experiments, in which the samples were heated in at least 12 temperature steps up to around 600 °C. All the heating procedures were conducted in air with a Natsuhara thermal demagnetizer, in which the residual field in the shield was maintained at less than 20 nT. Remanent magnetizations were measured with an AGICO spinner magnetometer. The natural remanent magnetization (NRM) intensities of most samples range from 1 to 8 A/m. Typical examples of demagnetization diagrams are shown in Fig. 2 by orthogonal projections of magnetization vectors. The NRMs of these samples mainly consist of one or two magnetization components. Low temperature components of the two-component samples seem to be the viscous remanences, which were removed at the low temperatures below ∼400 °C. Almost all of the stable ChRM components were unblocked at the temperatures between 550 and 600 °C, indicating that the NRMs are mainly carried by magnetite or Ti-poor titanomagnetite. However, some reddish samples from site AS1 showed much higher unblocking temperatures up to ∼635 °C (Fig. 2d), suggesting the existence of hematite. The demagnetization curves for the samples from site YM1 and AT, and some samples from AS1 were obtained from the demagnetization procedures included in the Thelliers' experiments (see Section 5).

All the ChRM directions show north-seeking declinations and positive inclinations, and are well clustered within each site and unit as summarized in Table 3. For calculations of the site-mean and the unit-mean directions, all the results from the ThD and Thelliers' experiments were used. In Table 3, the bracketed numerals show the number of the specimens used only for the ThD experiments and their directional data. Since they do not differ from the overall means, inclusion of the results from the Thelliers' experiments has no adverse effect. Some previous works also reported detailed paleomagnetic directions for these eruptive units, and their unit-mean directions are also given in Table 3. Fujii and Nakajima (1998) obtained the paleomagnetic directions using K-Ah ash flow deposits of northern Kyushu, and AT co-ignimbrite ash and pyroclastic flow deposits of several parts of Japan. And more recently, Fujii et al. (2001) reported the results obtained from welded tuffs in the four units of the Aso pyroclastic flow deposits of central Kyushu. For Aso-2, Shibuya et al. (1999) also determined the paleodirections using dense-welded pyroclastic flow deposits. A visualized comparison with equal area projections between the results of this study and the previous works is shown in Fig. 3. Our unit-mean directions closely agree with the well-grouped previous results from an enough number of the sites, suggesting that the ChRMs have been acquired in a short enough time interval. The unit-mean directions of AT, K-Ah, Aso-1, and -4 are reasonably close to the geocentric axial dipole (GAD) field direction of the sampling area (Fig. 3a and b), scattering within the range of secular variation. Relatively large easterly declinations for Aso-3

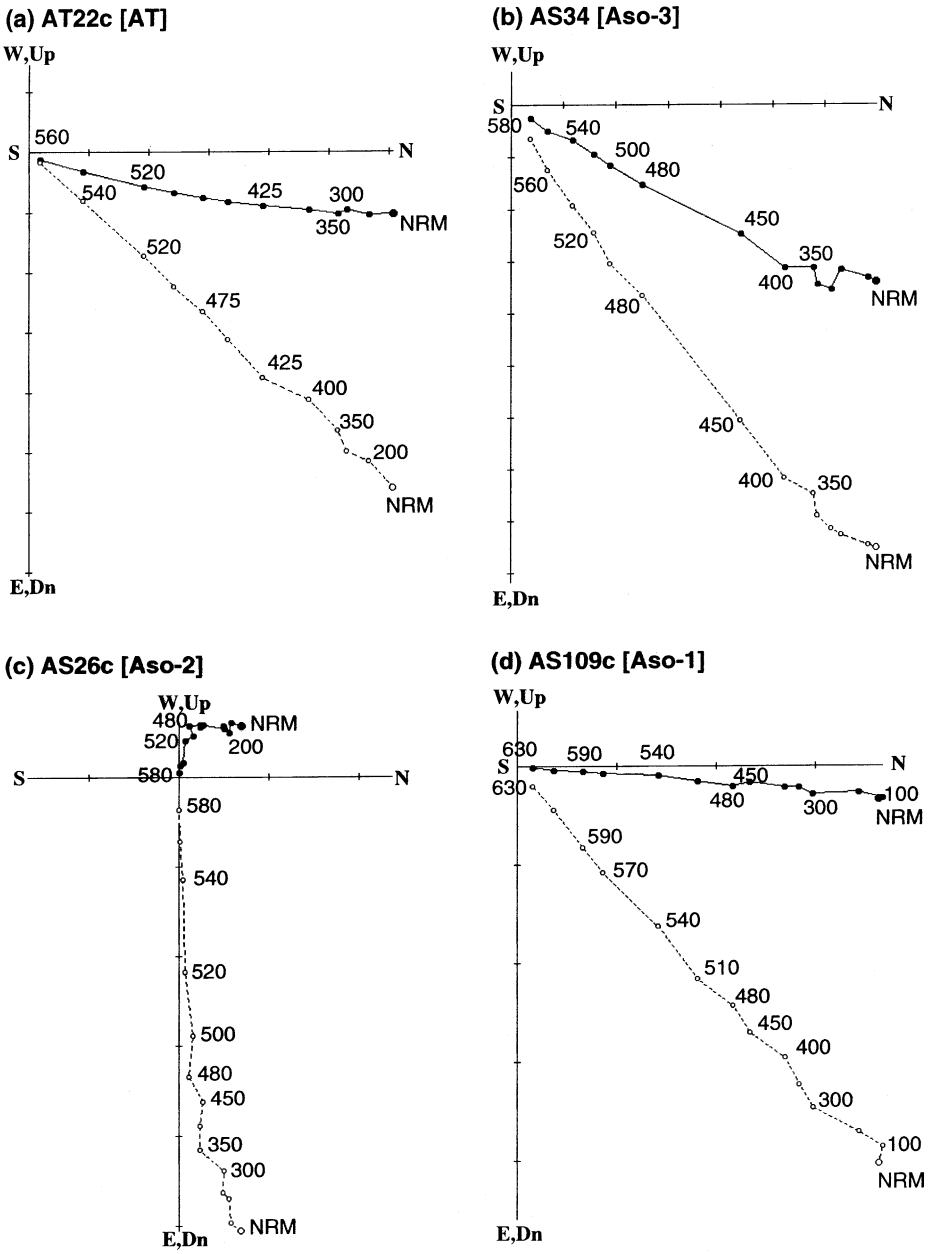

Fig. 2. Typical results of ThD. Open (solid) symbols represent the vector endpoints projected onto the vertical (horizontal) plane. Numbers beside the symbols represent temperatures (°C). The diagram for AT22c (a) was obtained by the demagnetization procedure included in the Thelliers' experiment.

(Fig. 3a and b) and abnormally steep inclinations for Aso-2 (Fig. 3c and d) are observed both in the present and previous results. For Aso-2, especially, a corresponding virtual geomagnetic pole (VGP) position calculated from our unit-mean direction is at 49°N, 119°E, which differs more than 40° from the geographic pole. This implies that Aso-2 might have recorded an excursion-like event.

Table 3
Summary of the paleomagnetic directions

Unit	Reference	Site	n	Dec (°)	Inc (°)	α_{95} (°)	k
K-Ah	This study	YM1	4 (0)	−6.1 (–)	46.4 (–)	4.8 (–)	369.4 (–)
	Fujii and Nakajima (1998)		3	2.5	52.3	4.2	865.3
AT	This study	AT	13 (0)	10.7 (–)	45.8 (–)	2.6 (–)	678.0 (–)
	Fujii and Nakajima (1998)		51	8.9	50.3	1.2	277.8
Aso-4	This study	IB	9 (3)	−2.9 (−2.5)	41.8 (42.3)	2.0 (6.6)	692.5 (345.4)
		ST	8 (2)	−5.5 (−4.6)	39.9 (38.5)	2.1 (7.3)	709.0 (1181.2)
		YM20	12 (4)	−6.7 (−6.7)	42.3 (41.3)	1.7 (12.7)	622.1 (386.3)
		Mean	3	−5.0 (−4.6)	41.3 (40.7)	2.9 (3.8)	1769.4 (1030.5)
	Fujii et al. (2001)		14	−5.2	42.0	2.4	271.0
Aso-3	This study	AS3	10 (2)	31.6 (27.8)	49.6 (49.8)	1.9 (20.3)	669.2 (1397.9)
		AY3	7 (1)	36.0 (35.2)	50.5 (52.9)	2.3	713.0
		Mean	2	33.8 (30.2)	50.1 (50.9)	6.5 (4.4)	1494.0 (523.2)
	Fujii et al. (2001)		9	35.7	51.0	3.5	216.7
Aso-2	This study	AY2	9 (2)	3.5 (5.9)	76.0 (76.3)	2.1 (2.6)	619.0 (8952.6)
		SD21	10 (3)	−80.3 (−85.1)	80.9 (81.0)	1.8 (1.9)	749.2 (4431.4)
		AS2	9 (2)	−31.4 (−41.9)	77.8 (79.6)	2.7 (25.6)	363.1 (97.5)
		SD20	9 (3)	−12.2 (−17.1)	82.6 (83.1)	2.3 (3.2)	500.9 (1474)
		Mean	4	−25.9 (−29.8)	80.8 (81.7)	7.8 (8.0)	138.5 (133.3)
	Fujii et al. (2001)		6	−6.6	76.4	4.7	204.9
	Shibuya et al. (1999)		6	9.1	78.8	4.4	235.0
Aso-1	This study	AS1	9 (0)	2.2 (–)	51.4 (–)	1.8 (–)	660.3 (–)
	Fujii et al. (2001)		5	3.4	49.0	5.2	217.6

n, number of specimens (or site-mean data); Dec, site (or unit)-mean declination; Inc, site (or unit) mean inclination; α_{95}, 95% confidence limit; k, precision parameter. For calculations of the mean paleomagnetic directions, all the results from ThD and Thelliers' experiments were used. Bracketed numerals show the number of specimens used only for ThD experiments and their directional data. Unit-mean directions from the previous reports by Fujii and Nakajima (1998), Shibuya et al. (1999), and Fujii et al. (2001) are also given.

4. Rock magnetism

To assess whether the samples are suitable for Thelliers' method, several rock magnetic properties of the samples were investigated. Hysteresis curve measurements and thermomagnetic analyses were carried out with a PMC MicroMag 3900 vibration sample magnetometer (VSM). As a result of these experiments, it was recognized that most of the samples are suitable for paleointensity determination.

4.1. Hysteresis measurements

Hysteresis loop parameters provide important information about the dominant magnetic minerals in rock samples and their grain size distribution. Hysteresis loops were measured with several samples for each site under a maximum magnetizing field of 500 mT. Fig. 4 shows typical examples of the hysteresis loops, in which paramagnetic components were subtracted assuming that the ferromagnetic components were saturated by 400 mT. Typical coercivity (Hc) values range from 6.3 to 33.9 mT, and these low Hc values are indicative that the dominant magnetic mineral contained in the samples is magnetite or titanomagnetite. Assuming that the dominant mineral is pure magnetite, its typical content in the samples derived from the saturation magnetization (Ms) is 0.25–2.1 wt.%. The observed hysteresis parameters of the samples from all units were plotted on a Day plot (Day et al., 1976, 1977) (Fig. 5). This magnetic domain-state diagram represented by Mrs/Ms versus Hrc/Hc (Mrs: saturation remanent magnetization; Hrc: remanent coercivity) was designed to estimate magnetic grain size. In this diagram, the critical values of SD–PSD and PSD–MD state transitions are represented by the lines

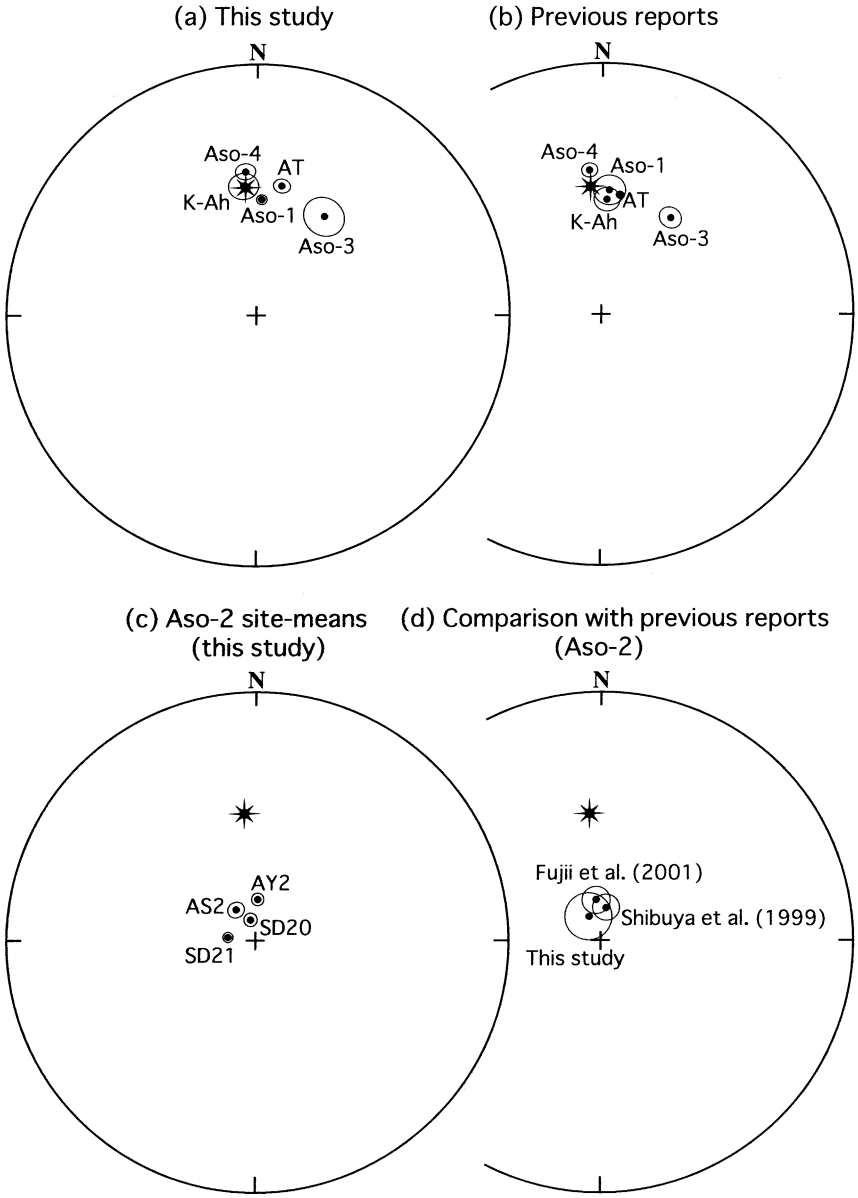

Fig. 3. Mean paleomagnetic directions with their 95% confidence limits. Solid circles are plotted on the lower hemisphere by an equal area projection. The star shows the present geomagnetic field direction of the sampling area. In situ unit-mean directions of K-Ah, AT, and Aso-1, -3, -4 by this study (a); the previous works (Fujii and Nakajima, 1998; Fujii et al., 2001) (b); in situ site-mean directions of Aso-2 by this study (c); comparison of the unit-mean directions of Aso-2 between this study and the previous reports (Shibuya et al., 1999; Fujii et al., 2001) (d).

(SD: single-domain; PSD: pseudo-single-domain; MD: multidomain). As shown in Fig. 5, the magnetic grain size of most of the samples is small enough to be in the PSD state, indicating that these samples can be used for paleointensity determinations by Thelliers' method. This result is consistent with the microscopic observations for these samples with a scanning electron microscope (SEM) that many lamellaes created by

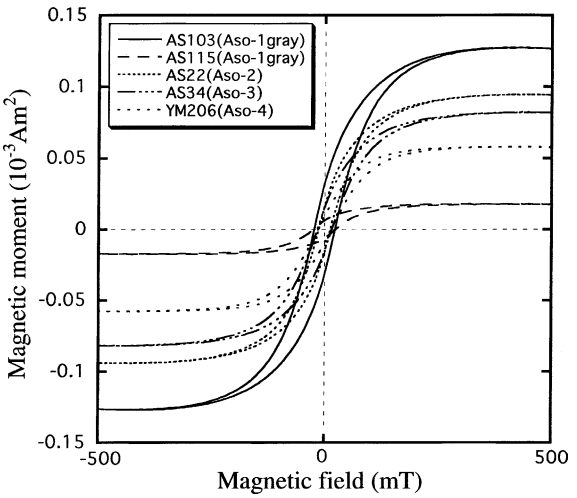

Fig. 4. Examples of the hysteresis loops at the room temperature. Paramagnetic components were subtracted.

high temperature oxidation divide the magnetic crystal into small sub-grains. The existence of the lamellaes is one of the evidences that these magnetic minerals can be stable carriers of TRM. The grain size of some of the Aso-4 samples is in the MD state or significantly separated from the PSD state. The SEM observations

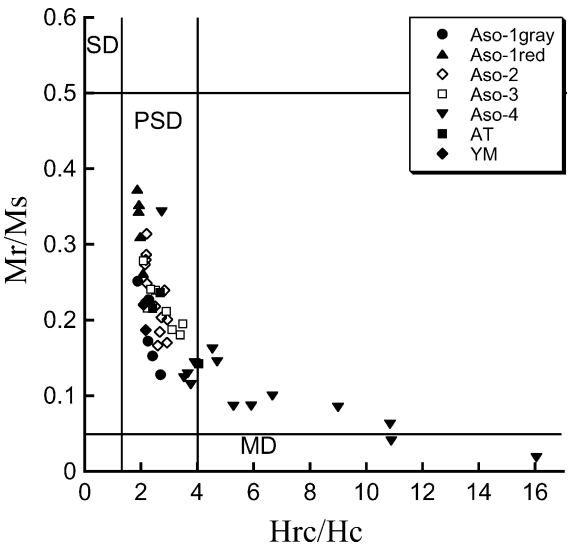

Fig. 5. The Day plot (Day et al., 1976, 1977) for the samples from all of the units. Domain states are represented in the regions enclosed by the lines. SD: single domain; PSD: pseudo-single domain; MD: multidomain.

also support that the magnetic grains in these samples have a large size of the order of 10–100 μm without lamellaes. Hence, for these samples, the results of paleointensity determination were not used for the calculation of the unit-mean paleointensity value.

4.2. High temperature measurements of rock magnetic properties

In order to determine Curie temperatures and constrain dominant magnetic minerals of the samples, we measured high field thermomagnetic curves in helium atmosphere with heating (up to 700 °C) and cooling rates of 35°C/min, applying a field of 500 mT. Fig. 6 shows some examples of the thermomagnetic curves. The Curie temperatures for the samples represented in Fig. 6a and b are around 580 °C, and most of the samples have a Curie temperature ranging between 550 and 595 °C. Thus, their magnetic careers are magnetite or Ti-poor titanomagnetite, and they seem to have been affected by high temperature oxidation. As mentioned above, this is also supported by the SEM observations which clarified the existence of the lamellaes in the magnetic grains. Reversible nature represented by Fig. 6a indicates that magnetic properties in this sample have been rarely affected by heating up to 700 °C. Fig. 6b shows an example of the irreversible curve, which results from chemical alteration of the sample by heating up to the high temperature of 700 °C. This behavior can be explained as Ti-poor regions formed during the in situ high temperature oxidation have been reduced to titanomagnetite of intermediate composition during the laboratory heating. As shown in Fig. 6c, the high Curie temperature of 635 °C indicates that hematite is also contained in this sample. This result was obtained from the reddish rock samples from site AS1, and is consistent with the result of ThD (see Section 3). Fig. 6a and c correspond to the grayish and reddish colored samples from the same site (AS1), respectively. Thus, the difference of magnetic minerals between those samples may be attributable to the difference in depositional environments (i.e. oxidizing or reducing conditions).

The degree of chemical alternation of the magnetic minerals during the laboratory heating was examined further for six samples by observing the hysteresis parameters after heating. Fig. 7 shows the normalized Ms values at the room temperature after stepwise heating

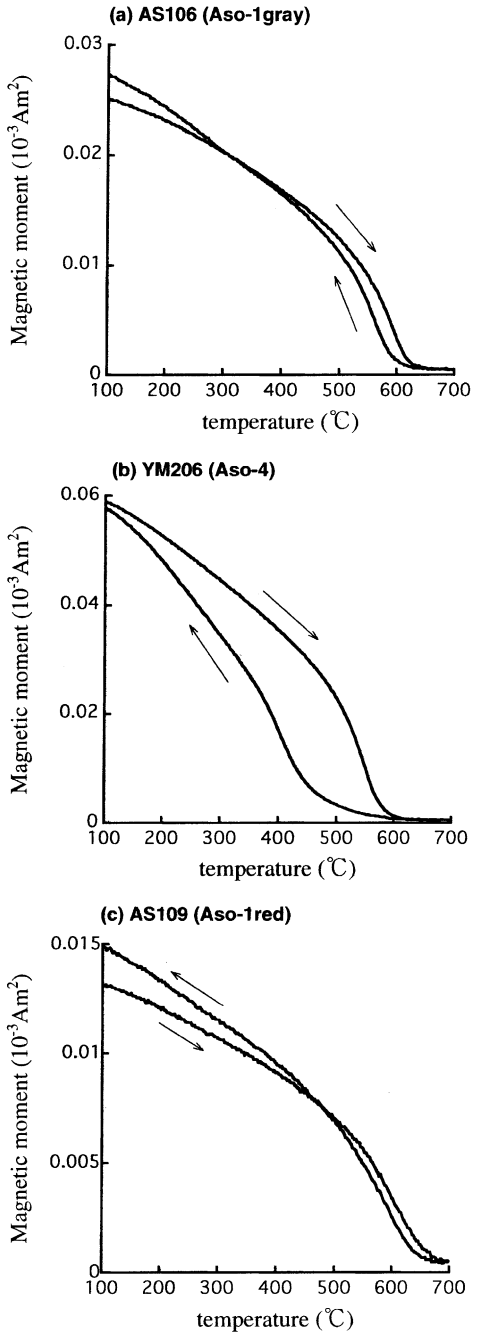

Fig. 6. Examples of the thermomagnetic curves. (a) Reversible curve from the grayish sample of Aso-1, showing a Curie temperature of 591 °C. (b) Irreversible curve from the sample of Aso-4, showing the Curie temperature of 570 °C. (c) Reversible curve from the reddish sample of Aso-1, showing a Curie temperature of 635 °C.

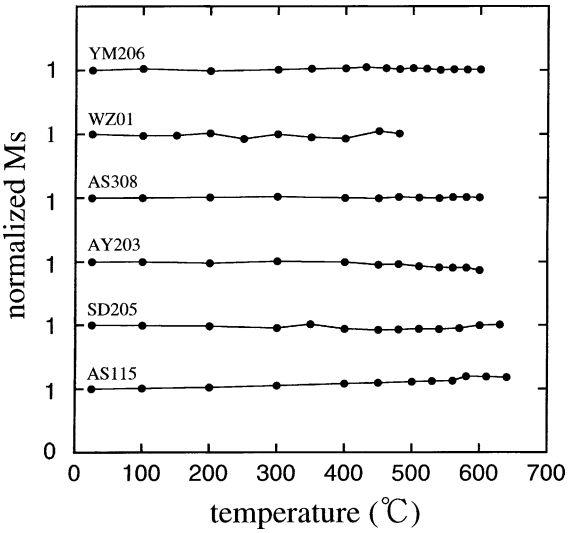

Fig. 7. Change in the Ms values derived from the room temperature hysteresis measurements after stepwise heating. The Ms values are normalized by the original value before heating.

up to 500–640 °C. Although no significant change in Ms value is observed in the temperature range up to 400 °C, the specimens from site AS1 (AS115) and AY2 (AY203) show considerable change due to chemical alteration after heating to temperatures higher than 500 and 600 °C, respectively, at which the Ms values increased more than 10% of the original values. Therefore, in the Thelliers' experiments for the samples from these two sites, the data points higher than 500 and 600 °C, respectively, were not used for the paleointensity determinations (see Section 5).

5. Paleointensity determinations

Paleointensity determinations were made for the samples of six eruptive units of dense welded pyroclastic flow deposits (15 sites), and we obtained successful results from the samples from 11 sites.

The technique used for the absolute paleointensity determinations is Coe's (1967) modified Thelliers' method. More than eight sequences of double heating procedures were carried out, and applied magnetizing field was controlled at 25, 30, or 40 μT, depending on the ability of TRM acquisition for each sample. In order to monitor possible chemical alterations by

laboratory heating, magnetic susceptibility measurements at room temperature were performed after each heating step with a Bartington MS-2 susceptibility meter. In addition, the pTRM (partial thermoremanent magnetization) test (Coe, 1967), which checks reproducibility of pTRMs, was carried out at least four times in the sequences of double heating. In the NRM–TRM diagram, in which the remaining NRM value was plotted versus the acquired TRM value for each heating step, a least-squares fitting was made for

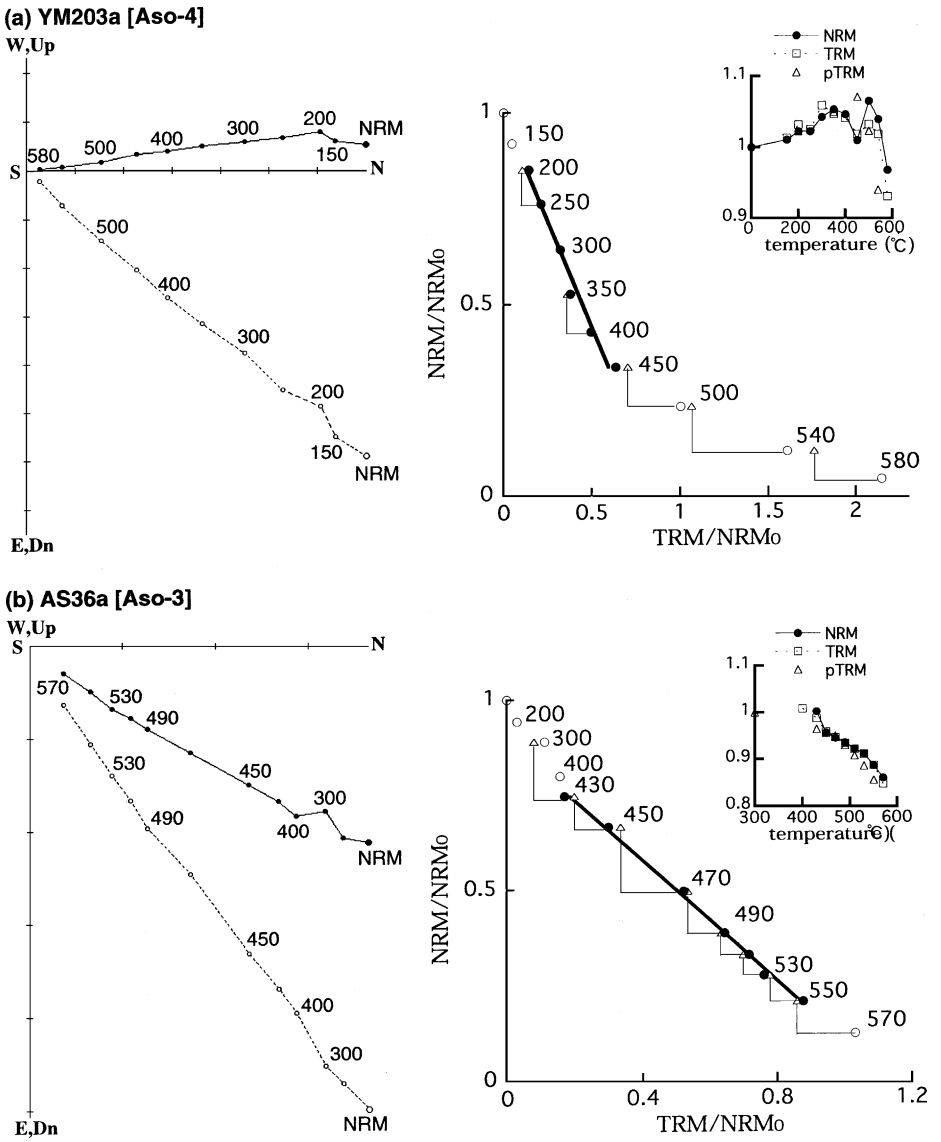

Fig. 8. Typical successful results of the Thelliers' experiments for YM2O3a (Aso-4) (a) and AS36a (Aso-3) (b). The demagnetization curves (left) and NRM–TRM diagrams (right) with the results of susceptibility measurements (right-upper inset). In the NRM–TRM diagram, units of the NRM and TRM axes are normalized by the original NRM intensity, NRM_0. Solid (open) circles indicate the data points used (rejected) for the straight-line fitting. Numbers beside the points show temperature steps (°C). Open triangles show the data points of the pTRM test. Susceptibility values (χ) are normalized by the original value (χ_0).

the data points corresponding to the ChRM with the treatment by York (1966, 1968). The criteria for data analysis were based on the following three tests. (1) The change in susceptibility after each heating step should be less than 20% of the original value. (2) In the linear segment, the pTRMs should be reproduced within the experimental errors of the previously acquired TRMs at the same temperature. The experimental errors were estimated with the method proposed by Kono and Tanaka (1984), in which we used the error estimates for various sources, such as errors in applied magnetic field control of 0.1 μT, in intensity measurement of 2.5%, in direction measurement of 2.5°, etc. (3) The linear segment should consist of more than four data points, and their correlation coefficient should exceed 0.99.

Two typical successful examples are shown in Fig. 8, in which the demagnetization curves (left) and the NRM–TRM diagrams (right) with the results of susceptibility measurements (right-upper inset) for sample YM2O3a (a) and AS36a (b) are represented. The data in the NRM–TRM diagram and the susceptibility values were normalized by the original values of NRM and susceptibility before heating, respectively.

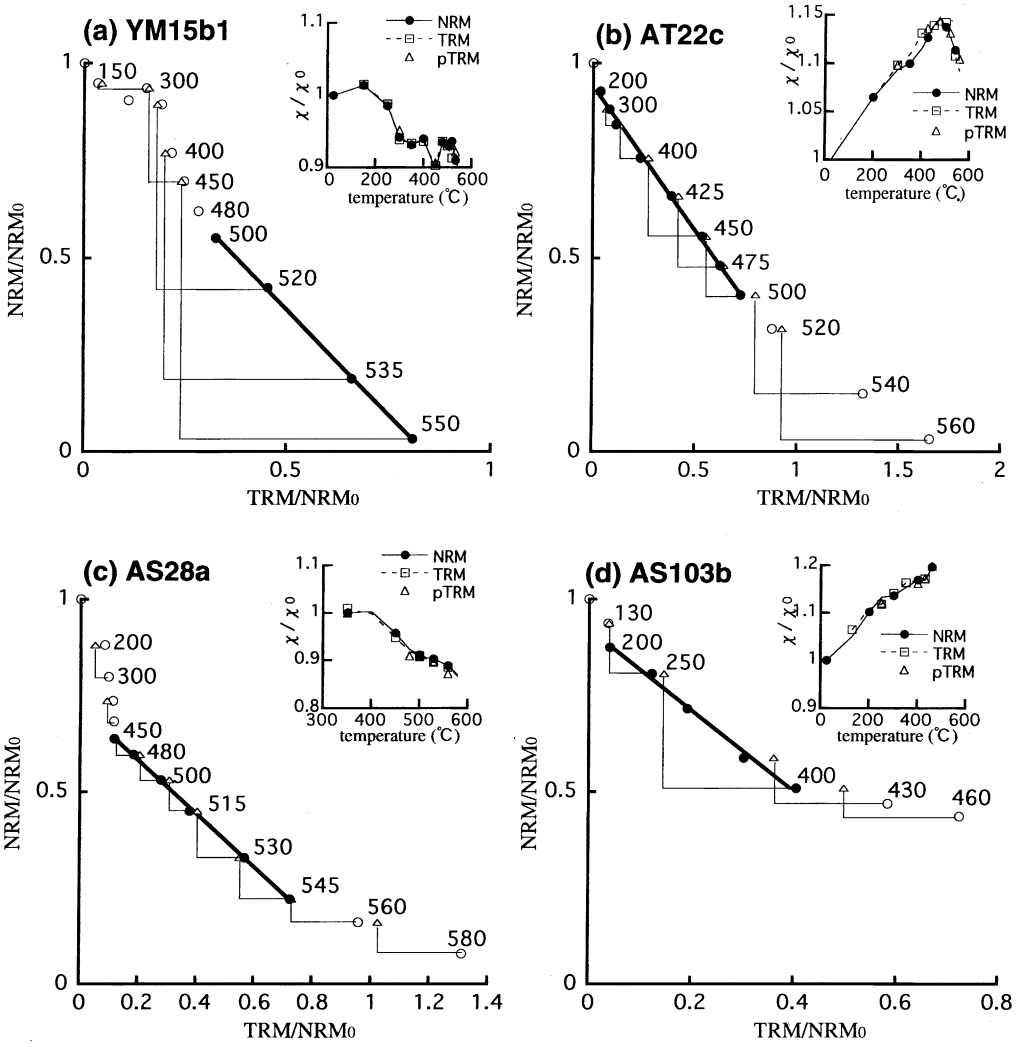

Fig. 9. NRM–TRM diagrams of typical successful results from K-Ah (a), AT (b), Aso-2 (c), and Aso-1 (d).

The linear segments used for paleointensity determination were drawn with the solid data points in the diagrams, and the results of the pTRM test were indicated by the open triangles. In Fig. 8, the demagnetization curves of YM2O3a (a) and AS36a (b) show that the low temperature components up to 150 and 400 °C, respectively, contain the secondary magnetizations. Hence, the data points of these temperature ranges were rejected for the straight-line fittings in the diagrams. We also rejected the data points above 450 °C for YM2O3a (a), and the points of 400 and 570 °C for AS36a (b) because these data reduce the correlation coefficients to less than 0.99, although some of them pass the pTRM test and the susceptibility values of these samples did not change more than 20% of the original values. Typical successful examples of the NRM–TRM diagram for another four units are shown in Fig. 9. We selected the temperature ranges for the straight-line fitting using the same procedures as explained above. As shown in most of the diagrams, a few data points at higher temperatures deviate from the fitted straight line, and some of them show large changes in susceptibility and negative results of the pTRM test. For example, in Fig. 9d, the data points of 430 and 460 °C did not pass the pTRM test due to the chemical alteration by the repeated heating, showing relatively large change in susceptibility. Thus, these data points were not used for the straight-line fitting.

Summary of the results is given in Table 4. For each sample, the slope of the linear segment, b, the standard error of the slope, σ_b, and the correlation coefficient, r, were calculated. The factors f (fraction of total extrapolated NRM spanned by the linear segment), g (gap factor for the data points in the linear segment), and q (combination of these parameters defined as $q = |b|fg/\sigma_b$) relating to the quality of the paleointensity determination, and weighted site-mean intensities were also calculated following the algorithm given by Coe et al. (1978). The samples with a large magnetic grain size (larger than PSD state) did not pass the criteria, except for the samples from site ST. Although the samples from site ST seem to have yielded plausible paleointensity values, they were not used for the calculation of the unit-mean intensity. For AT, we examined the effect of anisotropy of TRM acquisition on the paleointensity results using three samples, AT01, AT02 and AT25. Two or three cylindrical specimens were taken from each core sample, and one of them was placed in the magnetizer so that the axis of symmetry of the specimen was perpendicular to the magnetizing field direction. And the other specimens were magnetized in a direction parallel to their axes of symmetry. As shown in Table 4, no significant difference in the paleointensity values between the specimens can be recognized for these three samples, suggesting that the paleointensity results from AT were hardly affected by anisotropy of TRM acquisition.

As summarized in Table 4, similarity of the paleointensity values obtained from each site and unit suggests that the experiments were carried out accurately. The unit-mean intensity values calculated from the unweighted site-means for K-Ah, AT, Aso-4, -3, -2 and -1 are 37.8 ± 6.6, 23.6 ± 1.2, 45.9 ± 5.2, 31.8 ± 3.6, 20.4 ± 3.8 and 31.0 ± 3.4 μT, respectively.

6. Discussions

6.1. Comparison with other paleointensity records

The eruptive unit-mean paleointensity values of K-Ah, AT, Aso-4, -3, -2 and -1 yield the virtual dipole moment (VDM) values of (7.6 ± 1.3), (4.8 ± 0.2), (9.7 ± 1.1), (6.1 ± 0.7), (2.7 ± 0.5), and (5.9 ± 0.6) × 10^{22} A m^2, respectively (Table 4). For the VDM calculation, the unit-mean inclinations of the respective units were used. Except for Aso-2, the mean inclination for each unit is almost the same as that of the GAD field at the sampling area. Hence, there is no difference between the VDM and the virtual axial dipole moment (VADM) for these five units (Table 4). On the other hand, the VADM of 3.8 × 10^{22} A m^2 for Aso-2 is slightly larger than the VDM because of its abnormally steep inclination.

In Fig. 10, we plotted our VDM results as a function of age and compared with other volcanic and sedimentary paleointensity data. Fig. 10a includes absolute paleointensities extracted from the most recent available compilation of paleointensity so-called ‘Montpellier 1998’ database (Perrin et al., 1998), and recently published data from Kohala Mountain, Hawaii (Brassart et al., 1997) and La Guadeloupe Island, French West Indies (Carlut and Quidelleur, 2000). Fig. 10b shows the comparison with the global composite curve called Sint-800 constructed by Guyodo and Valet (1999), which is a stack of 33 relative paleointensity records.

Table 4
Summary of the paleointensity results

Unit	Sample	ΔT (°C)	n	r	b	H_{lab} (μT)	σ_b/b	f	g	q	H (μT)	Mean (μT) (weighted)	VADM (10^{22} A m^2)	VDM (10^{22} A m^2)
K-Ah	YM11a1	500–550	4	−0.9945	−0.697	40	0.0742	0.523	0.631	4.45	27.88	37.8 ± 6.6 (37.5 ± 3.8)		
	YM14a2	500–550	4	−1.0000	−0.896	40	0.0065	0.385	0.622	36.75	35.84			
	YM15b2	500–550	4	−0.9998	−1.075	40	0.0147	0.576	0.648	25.37	43.00			
	YM17a3	500–550	4	−0.9939	−1.111	40	0.0779	0.490	0.663	4.16	44.44			
K-Ah mean												37.8 ± 6.6	7.3 ± 1.3	7.6 ± 1.3
AT	AT01a1	300–500	4	−0.9971	−0.743	30	0.0543	0.529	0.646	6.30	22.29	23.6 ± 1.2 (23.5 ± 0.3)		
	AT01b1	300–500	4	−0.9994	−0.834	30	0.0253	0.469	0.649	12.03	25.02			
	AT02b1	300–500	4	−0.9981	−0.748	30	0.0436	0.483	0.649	7.20	22.44			
	AT02b2	300–500	4	−0.9994	−0.752	30	0.0254	0.449	0.639	11.28	22.56			
	AT02c2	200–500	5	−0.9991	−0.790	30	0.0241	0.261	0.659	7.13	23.70			
	AT21b	300–470	4	−0.9999	−0.786	30	0.0084	0.435	0.659	34.05	23.58			
	AT22c	200–500	8	−0.9987	−0.738	30	0.0210	0.548	0.838	21.91	22.14			
	AT23a	300–470	4	−0.9988	−0.748	30	0.0343	0.332	0.659	6.38	22.44			
	AT25c	200–500	8	−0.9980	−0.839	30	0.0256	0.388	0.828	12.53	25.17			
	AT25d	300–470	4	−0.9996	−0.782	30	0.0197	0.291	0.570	8.40	23.46			
	AT26a	200–500	8	−0.9990	−0.868	30	0.0178	0.348	0.802	15.65	26.04			
	AT27b	300–470	4	−0.9996	−0.783	30	0.0211	0.391	0.656	12.15	23.49			
	AT28b	350–450	4	−0.9998	−0.797	30	0.0141	0.292	0.658	13.60	23.91			
AT mean												23.6 ± 1.2	4.5 ± 0.2	4.8 ± 0.2
Aso-4B	IB422b	350–520	5	−0.9917	−0.955	40	0.0746	0.415	0.730	4.06	38.20	42.4 ± 7.0 (39.6 ± 3.4)		
	IB423b	350–490	4	−0.9930	−1.432	40	0.0838	0.254	0.658	2.00	57.28			
	IB424b	410–520	4	−0.9908	−0.971	40	0.0959	0.312	0.667	2.17	38.84			
	IB425b	410–530	5	−0.9937	−1.091	40	0.0647	0.383	0.747	4.42	43.64			
	IB427b	350–520	5	−0.9939	−0.928	40	0.0638	0.390	0.733	4.48	37.12			
	IB428b	350–520	5	−0.9945	−0.978	40	0.0606	0.396	0.733	4.79	39.12			
	ST41b*	380–490	5	−0.9949	−1.299	40	0.0584	0.410	0.728	5.11	51.96	43.8 ± 9.1* (43.9 ± 4.1)		
	ST42b*	380–470	4	−0.9920	−0.918	40	0.0895	0.274	0.656	2.01	36.72			
	ST43b*	380–470	4	−0.9984	−0.716	40	0.0405	0.334	0.663	5.47	28.64			
	ST46b*	380–520	6	−0.9954	−1.030	40	0.0481	0.573	0.793	9.44	41.20			
	ST47b*	350–490	6	−0.9979	−1.357	40	0.0320	0.501	0.788	12.32	54.28			
	ST48c*	380–510	6	−0.9935	−1.249	40	0.0568	0.487	0.795	6.81	49.96			
Aso-4B mean												42.4 ± 7.0		
Aso-4A	YM201b	200–400	5	−0.9986	−1.254	40	0.0301	0.449	0.739	11.02	50.16	49.4 ± 3.3 (46.7 ± 1.6)		
	YM202b	150–400	6	−0.9996	−1.177	40	0.0150	0.472	0.788	24.77	47.08			
	YM203a	200–400	5	−0.9938	−1.247	40	0.0642	0.418	0.743	4.85	49.88			
	YM204a	200–400	5	−0.9993	−1.216	40	0.0223	0.349	0.743	11.65	48.64			
	YM205a	150–400	6	−0.9992	−1.211	40	0.0206	0.457	0.787	17.50	48.44			

Table 4 (*Continued*)

Unit	Sample	ΔT (°C)	n	r	b	H_{lab} (μT)	σ_b/b	f	g	q	H (μT)	Mean (μT) (weighted)	VADM (10^{22} A m^2)	VDM (10^{22} A m^2)
	YM206a	150–350	5	−0.9915	−1.429	40	0.0752	0.342	0.736	3.35	57.16			
	YM207c	200–450	6	−0.9921	−1.234	40	0.0628	0.626	0.796	7.94	49.36			
	YM208b	150–400	6	−0.9996	−1.119	40	0.0142	0.489	0.785	27.06	44.76			
Aso-4A mean												49.4 ± 3.3		
Aso-4 mean												45.9 ± 5.2	8.6 ± 1.0	9.7 ± 1.1
Aso-3	AS31b	455–525	6	−0.9973	−0.917	30	0.0368	0.417	0.783	8.85	27.51	30.5 ± 1.8 (30.5 ± 0.7)		
	AS32b	430–570	8	−0.9952	−0.746	40	0.0398	0.764	0.802	15.40	29.84			
	AS33a	430–540	9	−0.9973	−1.078	30	0.0276	0.586	0.866	18.39	32.34			
	AS35a	455–540	7	−0.9983	−1.051	30	0.0262	0.435	0.807	13.38	31.53			
	AS35c	450–550	6	−0.9995	−0.741	40	0.0164	0.530	0.731	23.66	29.64			
	AS36a	430–550	7	−0.9984	−0.794	40	0.0253	0.616	0.799	19.41	31.76			
	AS37b	430–570	6	−0.9972	−0.717	40	0.0375	0.738	0.685	13.47	28.68			
	AS38a	455–540	7	−0.9972	−1.099	30	0.0336	0.433	0.810	10.44	32.97			
	AY31b	445–580	9	−0.9987	−0.953	30	0.0189	0.805	0.864	36.73	28.59	33.1 ± 5.1 (29.4 ± 2.8)		
	AY32b	510–570	4	−0.9931	−1.066	40	0.0832	0.295	0.621	2.20	42.64			
	AY33a	490–570	5	−0.9964	−0.728	40	0.0488	0.591	0.707	8.56	29.12			
	AY34c	490–570	5	−0.9985	−0.930	40	0.0318	0.574	0.710	12.79	37.20			
	AY35a	445–560	8	−0.9986	−0.981	30	0.0220	0.797	0.844	30.60	29.43			
	AY36a	490–580	7	−0.9954	−1.063	30	0.0428	0.656	0.811	12.44	31.89			
Aso-3 mean												31.8 ± 3.6	6.0 ± 0.7	6.1 ± 0.7
Aso-2B	AY21a	450–560	7	−0.9934	−0.756	25	0.0515	0.635	0.814	10.04	18.90	19.1 ± 1.7 (17.9 ± 0.9)		
	AY23b	480–560	6	−0.9959	−0.781	25	0.0451	0.566	0.784	9.85	19.53			
	AY24a	515–560	4	−0.9997	−0.541	30	0.0179	0.423	0.655	15.53	16.23			
	AY25c	400–545	7	−0.9967	−0.867	25	0.0363	0.426	0.823	9.68	21.68			
	AY26b	450–545	6	−0.9980	−0.649	30	0.0315	0.365	0.782	9.05	19.47			
	AY27b	450–545	6	−0.9993	−0.694	25	0.0181	0.416	0.788	18.10	17.35			
	AY28c	350–545	8	−0.9913	−0.689	30	0.0537	0.481	0.827	7.41	20.67			
	SD213b	300–520	6	−0.9907	−0.663	25	0.0684	0.373	0.777	4.24	16.58	18.6 ± 1.9 (18.6 ± 0.8)		
	SD212b	390–540	6	−0.9974	−0.692	25	0.0362	0.293	0.793	6.41	17.30			
	SD214c	350–540	7	−0.9985	−0.627	25	0.0243	0.348	0.824	11.82	15.68			
	SD215b	300–520	6	−0.9912	−0.840	25	0.0665	0.366	0.788	4.33	21.00			
	SD216b	300–540	8	−0.9979	−0.767	25	0.0267	0.418	0.853	13.35	19.18			
	SD217b	300–520	7	−0.9989	−0.831	25	0.0205	0.364	0.826	14.65	20.78			
	SD218b	300–550	7	−0.9979	−0.784	25	0.0289	0.541	0.815	15.23	19.60			
Aso-2B mean												18.9 ± 1.8		
Aso-2A	AS21b	450–545	6	−0.9985	−0.622	30	0.0278	0.664	0.779	18.59	18.66	17.9 ± 1.0 (17.5 ± 0.4)		
	AS22a	400–545	7	−0.9985	−0.577	30	0.0245	0.591	0.793	19.16	17.31			

	AS23b	450–545	6	−0.9993	−0.645	30	0.0182	0.564	0.779	24.11	19.35			
	AS24c	450–530	5	−0.9996	−0.627	30	0.0160	0.389	0.738	17.96	18.81			
	AS25a	450–545	6	−0.9975	−0.687	25	0.0352	0.596	0.789	13.34	17.18			
	AS27a	480–545	5	−0.9998	−0.662	25	0.0122	0.505	0.737	30.57	16.55			
	AS28a	450–545	6	−0.9996	−0.688	25	0.0145	0.581	0.775	31.11	17.20			
	SD201b	200–350	4	−0.9967	−1.237	25	0.0578	0.287	0.654	3.25	30.93	25.8 ± 7.4 (17.6 ± 5.0)		
	SD202b	200–390	5	−0.9963	−1.211	25	0.0494	0.390	0.747	5.90	30.28			
	SD204b	200–350	4	−0.9962	−1.403	25	0.0617	0.261	0.658	2.79	35.08			
	SD205a	200–415	6	−0.9816	−1.077	25	0.0960	0.411	0.797	3.41	26.93			
	SD206b	250–500	8	−0.9914	−0.629	25	0.0534	0.726	0.804	10.92	15.73			
	SD208b	350–460	4	−0.9911	−0.643	25	0.0943	0.158	0.666	1.12	16.08			
Aso-2A mean												21.8 ± 5.3		
Aso-2 mean												20.4 ± 3.8	3.8 ± 0.7	2.7 ± 0.5
Aso-1gray	AS103b	200–400	5	−0.9965	−1.041	30	0.0482	0.405	0.741	6.23	31.23	31.0 ± 3.4 (28.9 ± 1.4)		
	AS105b	200–400	5	−1.0000	−1.043	30	0.0056	0.435	0.738	57.37	31.29			
	AS106b	200–400	5	−0.9996	−0.995	30	0.0164	0.434	0.732	19.37	29.85			
	AS107b	200–400	5	−0.9997	−0.967	30	0.0129	0.381	0.744	21.95	29.01			
Aso-1red	AS109b	200–450	4	−1.0000	−0.637	40	0.0039	0.249	0.654	41.58	25.48			
	AS114b	200–450	4	−0.9954	−1.257	30	0.0676	0.195	0.661	1.91	37.71			
	AS114c	200–450	4	−0.9994	−0.876	40	0.0237	0.186	0.663	5.19	35.04			
	AS115b	200–450	4	−0.9999	−0.719	40	0.0106	0.243	0.656	15.04	28.76			
	AS117b	200–450	4	−0.9990	−0.770	40	0.0322	0.215	0.647	4.32	30.80			
Aso-1 mean												31.0 ± 3.4	5.8 ± 0.6	5.9 ± 0.6

ΔT, temperature range of the linear segment; n, number of the data points in the linear segment; r, correlation coefficient of the linear relationship; b, slope of the linear segment; H_{lab}, magnetizing field intensity applied in the laboratory; σ_b/b, relative standard deviation of the slope; f, fraction of total extrapolated NRM spanned by the linear segment; g, gap factor for data points in the linear segment; q, quality factor of the paleointensity estimate; H, paleointensity obtained from each specimen. The site-means, weighted site-means, unit-means, VADMs, and VDMs with the standard deviations are also represented. The unit-mean values were calculated from the unweighted site-means. The values of f, g, q, and weighted site-mean were calculated with the algorithm given by Coe et al. (1978).

In Sint-800, the absolute scale is determined as VADM by fitting the relative intensity variation for the past 40 kyr with the absolute paleointensity data obtained from the volcanic rocks. In both graphs, the 1σ range of the averaged VDM value of $(7.8 \pm 3.4) \times 10^{22}$ A m^2 for the past 1 Myr calculated from the database is shown in gray. As shown in Fig. 10, the VDMs from K-Ah, AT, Aso-4, -3 and -1 do not differ much from the average value for the past 1 Myr, being within the 1σ range. The results from K-Ah and AT are perfectly consistent with the clear-cut trend that the dipole moment has been increasing for the past 40 kyr after the Laschamp event, which can be observed in both of volcanic and sedimentary records. For the absolute data older than 200 ka, as can be seen in Fig. 10a, most of the age controls seem to be much less certain than the younger ones, prohibiting us to characterize the dipole variation on time scales of the order of 10 kyr. The result from Aso-1 has large significance in that it is one of the best-dated absolute data with the ages older than 200 ka.

In the interval between 70 and 130 ka, almost all of the volcanic VDM values reside within the 1σ range of the average VDM for the past 1 Myr (Fig. 10a), and this compilation hardly recognizes such a duration of low dipole moments between 100 and 120 ka concerning the Blake event as displayed in Sint-800 curve (Fig. 10b). The numerous absolute paleointensity data obtained from a volcanic sequence of La Réunion Island (Chauvin et al., 1991; Raïs et al., 1996)

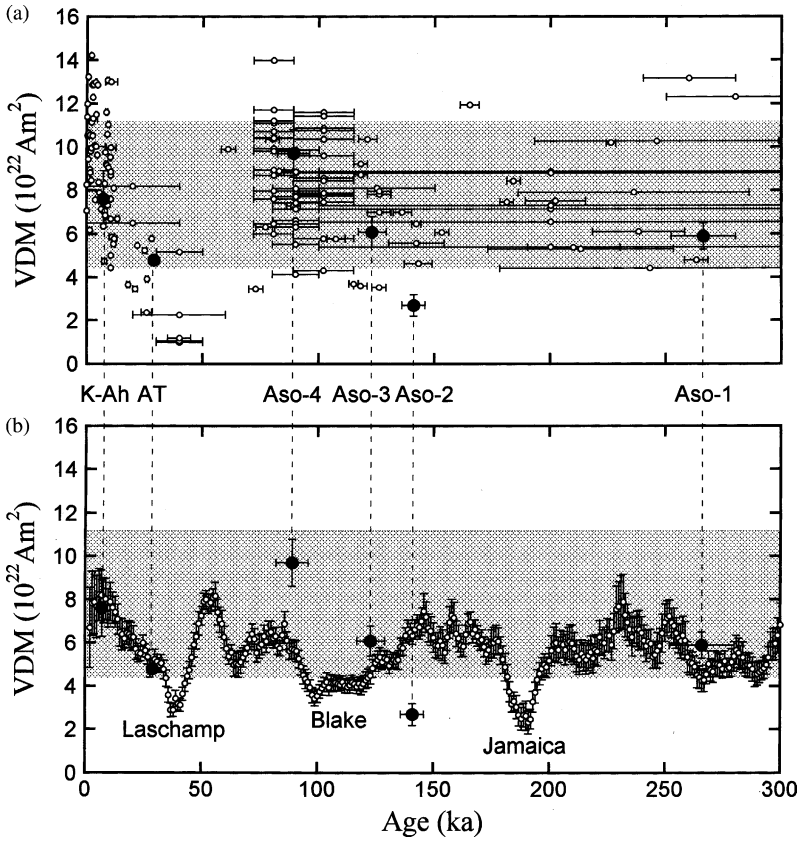

Fig. 10. Comparison with other volcanic and sedimentary paleointensity data. The VDM values obtained in this study are represented by the solid circles. (a) Comparison with the other volcanic data (open circles) extracted from the 'Montpellier 1998' database (Perrin et al., 1998), and recently published data from Hawaii (Brassart et al., 1997) and French West Indies (Carlut and Quidelleur, 2000). (b) Comparison with Sint-800 (Guyodo and Valet, 1999) (open circles). The absolute scale for Sint-800 was determined as VADM. The 1σ range of the averaged VDM for the past 1 Myr calculated from the database is shown in gray.

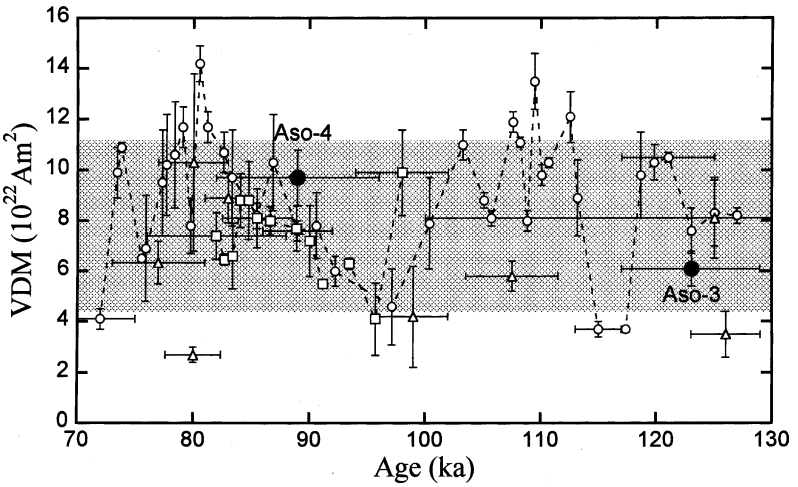

Fig. 11. Absolute VDM variation with the interpolated ages from La Réunion Island by Chauvin et al. (1991) (open squares) and Raïs et al. (1996) (open circles), and other available data for the period between 70 and 130 ka (open triangles) from Sicily (Tric et al., 1994), Germany (Schnepp, 1996), Hawaii (Brassart et al., 1997), French West Indies (Carlut and Quidelleur, 2000). The results from Aso-4 and -3 are shown by the solid circles. The 1σ range of the averaged VDM for the past 1 Myr calculated from the database is shown in gray.

are quite informative to investigate the variation of the dipole moments in this time interval in further detail. Raïs et al. (1996) observed a linear extrusion rate in their sampled section using K-Ar ages, and calculated an interpolated age for each lava flow. Following the same approach, we estimated an age for each cooling unit of Chauvin et al. (1991) and Raïs et al. (1996), assuming a constant extrusion rate between flows dated by K-Ar method. Fig. 11 shows the absolute VDM variation with the interpolated ages from La Réunion Island and other available data for the period between 70 and 130 ka from Sicily (Tric et al., 1994), Germany (Schnepp, 1996), Hawaii (Brassart et al., 1997), French West Indies (Carlut and Quidelleur, 2000), and Aso-4 and -3 (this study). One can see that the results of Aso-4 and -3 show remarkable agreement with the La Réunion Island results, although both areas are much separated from each other, and each value is considered to be a spot-measure of the geomagnetic field. The La Réunion Island results indicate two troughs of low dipole moments around 95 and 115 ka, which coincide with the duration of the Blake event documented in Sint-800 (Fig. 10b). Raïs et al. (1996) interpreted the observed vector change at 115 ka as a partial record of the Blake event. Hence, we conclude that the occurrence of Aso-3 was just before the Blake event, or at the beginning of this geomagnetic episode. The large east-seeking declination observed in Aso-3 also might imply that, at the time of the Aso-3 eruption, the non-dipole component were relatively strong compared with the dipole, being related to the beginning of the Blake event. As can be seen from Fig. 10b, there is a considerable difference between the Aso-4 result and the Sint-800 curve. However, all the absolute VDMs between 70 and 90 ka (Fig. 11) are significantly larger than the moments of Sint-800, suggesting that the amplitude of the intensity variation of Sint-800 for this time interval has been reduced due to the stacking of many sedimentary records.

6.2. *Excursion-like event recorded by Aso-2*

The result from Aso-2 requires special attention. Its low VDM value of $(2.7 \pm 0.5) \times 10^{22}$ A m^2 corresponds to about 35% of the mean value for the past 1 Myr (Fig. 10), and even taking the VADM of 3.8×10^{22} A m^2, the moment is much smaller than the average. Shibuya et al. (1999) previously reported low paleointensity values of the pyroclastic flow deposits of Aso-2 ranging from 23 to 27 μT, which are similar to the present results. In addition to its abnormal VGP (49°N, 119°E) position as described in Section 3, this weak intensity also supports the possibility that Aso-2 records an excursion-like event. As mentioned earlier,

we interpret that Aso-3 has occurred just before the Blake event, and there seems to be a considerable age difference between Aso-2 and the Jamaica event occurred around 180–190 ka (e.g. Champion et al., 1988). Therefore, we consider that the geomagnetic event recorded by Aso-2 cannot be correlated with these two previously known excursions. As shown in Fig. 10b, however, there is no significant intensity drop which corresponds to the low intensity obtained from Aso-2 between the Blake and Jamaica events in the Sint-800 curve.

We can give four possibilities to explain the invisibility of this geomagnetic episode in Sint-800. The first is that the evaluations of the constituent relative paleointensities themselves are incorrect, but this issue seems to be beyond the present discussion. The second is that the amplitude of the intensity variation of Sint-800 has been reduced due to the stacking of

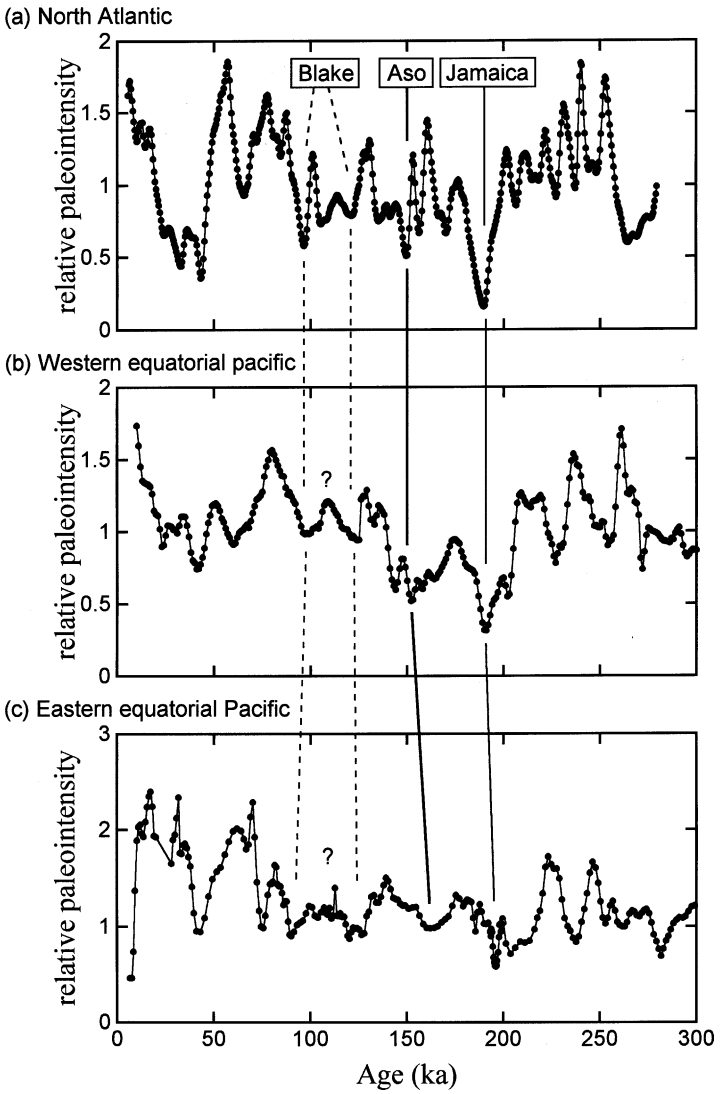

Fig. 12. Stacked relative paleointensity curves obtained from Açores area in north Atlantic (Lehman et al., 1996) (a), Ontong–Java in western equatorial Pacific (Tauxe and Shackleton, 1994) (b), and Leg. 138 in eastern equatorial Pacific (Meynadier et al., 1995) (c). The troughs interpreted as the Blake and Jamaica events, and the intensity drops with similar ages to that of Aso-2 are indicated by the lines.

many sedimentary records as mentioned above. The third is that the age scale for Sint-800 is in error. And the forth is that short-period variations in the Sint-800 curve have been smoothed out owing to the stacking. However, it is difficult to attribute the main cause of the invisibility to the second and third possibilities. All the other major excursions can be observed clearly in Sint-800, suffering reduction of the amplitude to some extent. It is also impossible to adjust the Sint-800 curve to the Aso-2 result by changing its age assignment. The age control for Sint-800 is based on oxygen isotope stages, which allow no significant errors more than ∼30 ka. The fourth seems much more likely, because short-period variations can be cancelled out through the stacking of a large number of records which contain uncertainty in age and amplitude.

By investigating all the source records of Sint-800 and some other reliable sedimentary records, we found the similar features to the result from Aso-2 in most of them. Following three records are good examples; stacked relative paleointensity curves obtained from Ontong–Java in western equatorial Pacific (the results from core ERDC-113p and RNDB-75p are contained in Sint-800) by Tauxe and Shackleton (1994), Leg. 138 in eastern equatorial Pacific (core ODP851 in Sint-800) by Meynadier et al. (1995), and Açores area in north Atlantic (core SU92-18 and 19 in Sint-800) by Lehman et al. (1996). The results from these three areas are shown in Fig. 12. In each record, one can see an obvious intensity drop between two durations of the low intensities around 90–120 ka and around 190 ka, which can be interpreted as the Blake and Jamaica events, respectively. The age of the intensity drop closely agrees with that of Aso-2 of 140 ka. Among the 16 boring sites, the records from six sites show this intensity drop obviously. The slight drop can be observed in another eight sites, and only the two other sites do not show such event. Supposing that this intensity drop around 150–160 ka represents the same event as the excursion-like event of Aso-2, we propose to name it ‘Aso event’. As well as the intensity drop, rapid changes in the paleomagnetic direction, especially in inclination, between the Blake and Jamaica events have also been observed in some of the sedimentary records (e.g. Yamazaki and Ioka, 1994; Lehman et al., 1996). Moreover, apart from the relative intensity records, an excursion event around 150–160 ka has been reported by several paleodirectional secular variation records from Alaska (Weatgate, 1988; Gillen and Evans, 1989), Arctic Ocean Nowaczyk and Baumann, 1992; Nowaczyk et al., 1994), and South China Sea (Lee, 1999). Nowaczyk et al. (1994) categorized the excursion discovered at Alaska and Arctic Ocean as ‘Baffin Bay event’, and Peate et al. (1996) prefer to call it ‘Old Crow event’. The Aso event might be correlated with the Baffin Bay (Old Crow) event.

7. Conclusions

A detailed paleomagnetic study was undertaken on welded pyroclastic flow deposits co-born with widespread tephras derived from Kikai (K-Ah, 7.3 ka), Aira (AT, 28 ka), and Aso (Aso-1, 270 ka; Aso-2, 140 ka; Aso-3, 120 ka; Aso-4, 90 ka) calderas in Kyushu Island, Japan. Thermal demagnetization shows that these pyroclastic flow deposits have stable ChRM components, and their directions are consistent with the results of the previous paleodirectional works (Fujii and Nakajima, 1998; Shibuya et al., 1999; Fujii et al., 2001). Several rock magnetic measurements indicate that their main magnetic careers are magnetite or Ti-poor titanomagnetite with the grain size small enough to be in the PSD state, and that their magnetic properties are hardly affected by laboratory heating.

Paleointensity determinations by Thelliers’ method with the pTRM test were carried out for the samples of six units of pyroclastic flow deposits, and reliable results were obtained from them. The VDM values for the youngest units of K-Ah and AT are consistent with the clear-cut global trend of increasing dipole moment for the past 40 kyr after the Laschamp event observed in the previous volcanic and sedimentary records. Aso-4, -3 and -1 yield the moderate VDMs similar to the averaged absolute VDM value for the past 1 Myr, and especially, the results from Aso-4 and -3 show remarkable agreement with the paleointensity variation for the interval between 70 and 130 ka obtained from La Réunion Island (Chauvin et al., 1991; Raïs et al., 1996). The low VDM value and abnormal VGP position obtained from Aso-2 suggest a possibility that Aso-2 records an excursion-like event around 140 ka. Although a corresponding intensity drop cannot be observed in Sint-800, we found the similar features to the Aso-2 result in some of the individual sedimentary records around 150–160 ka.

Acknowledgements

We would like to express our cordial thanks first to Mr. Y. Iwasaki of Kumamoto Univ. for his extensive support throughout this study. We thank also Kawasaki Geological Engineering Co. Ltd., Mr. Y. Kudo of Toyooka Primary School, Dr. M. Torii, Ms. M. Siihara, Prof. Y. Hase, Dr. H. Yokose and the members of his research group of Kumamoto University for their support in the sampling and the geological guidance. Prof. I. Kaneoka of the Earthquake Research Institute of the University of Tokyo and Dr. T. Yamazaki of AIST are thanked for their fruitful suggestions and discussions, and Dr. M. Kono and Dr. M. Gratton for their helpful comments on the manuscript. Mr. T. Ushikubo and the 3rd grade students of the rock magnetism group of the geophysical experimental course of the University of Tokyo are thanked for their help in the experiments.

References

Brassart, J., Tric, E., Valet, J.P., Herrero-Bervera, E., 1997. Absolute paleointensity between 60 and 400 ka from Kohala Mountain (Hawaii). Earth Planet. Sci. Lett. 148, 141–156.

Carlut, J., Quidelleur, X., 2000. Absolute paleointensities recorded during the Brunhes chron at La Guadeloupe Island. Phys. Earth Planet. Inter. 120, 255–269.

Champion, D.E., Lanphere, M.A., Kuntz, M.A., 1988. Evidence for a new geomagnetic reversal from lava flows in Idaho: discussion of short polarity reversals in the Brunhes and late Matsuyama polarity chrons. J. Geophys. Res. 93, 11667–11680.

Chauvin, A., Gillot, P.Y., Bonhommet, N., 1991. Paleointensity of the Earth's magnetic field recorded by two late quaternary volcanic sequences at the Island of La Réunion. J. Geophys. Res. 96, 1981–2006.

Coe, R.S., 1967. Paleo-intensities of Earth's magnetic field determined from tertiary and quaternary rocks. J. Geophys. Res. 72, 3247–3262.

Coe, R.S., Gromme, S., Manskinen, E.A., 1978. Geomagnetic paleointensities from radiocarbon-dated lava flows on Hawaii and the question of the Pacific non-dipole low. J. Geophys. Res. 83, 1740–1756.

Day, R., Fuller, M., Schmidt, V.A., 1976. Magnetic hysteresis properties of synthetic titanomagnetites. J. Geophys. Res. 81, 873–880.

Day, R., Fuller, M., Schmidt, V.A., 1977. Hysteresis properties of titanomagnetites: grain size and composition dependence. Phys. Earth Planet. Inter. 13, 260–267.

Fujii, J., Nakajima, T., 1998. Paleomagnetic directions of quaternary widespread tephras. Mem. Fac. Edu. Fukui Univ., Ser. II 51, 47–60 (in Japanese with English abstract).

Fujii, J., Nakajima, T., Kamata, H., 2001. Paleomagnetic directions of the Aso pyroclastic-flow and the Aso-4 co-ignimbrite ash-fall deposits in Japan. Earth Planet. Space 53, 1137–1150.

Gillen, K.P., Evans, M.E., 1989. New geomagnetic paleosecular-variation results from the Old Crow Basin, Yukon Territory, and their use in stratigraphic correlation. Can. J. Earth Sci. 26, 2507–2511.

Guyodo, Y., Valet, J.P., 1999. Global changes in intensity of the Earth's magnetic field during the past 800 kyr. Nature 399, 249–252.

Kitagawa, H., Plicht, J.V.D., 1998. Atmospheric radiocarbon calibration to 45,000 years. B.P.: late glacial fluctuations and cosmogenic isotope production. Science 279, 1187–1190.

Kono, M., Tanaka, H., 1984. Analysis of the Thelliers' method of paleointensity determination. 1. Estimation of statistical errors. J. Geomagn. Geoelectr. 36, 267–284.

Lee, T.Q., 1999. Last 160 ka paleomagnetic directional secular variation record from core MD972151, southwestern South China Sea. TAO 10 (1), 255–264.

Lehman, B., Laj, C., Kissel, C., Mazaud, A., Paterne, M., Labeyrie, L., 1996. Relative changes of the geomagnetic field intensity during the last 280 kyears from piston cores in the Açres area. Phys. Earth Planet. Inter. 93, 269–284.

Matsumoto, T., Uto, K., Ono, K., Watanabe, K., 1991. K-Ar age determinations for Aso volcanic rocks: concordance with volcanostratigraphy and application flow. In: Proceedings of the Fall Meeting of the Volcanological Society, Japan, p. 73 (in Japanese, Abstracts).

Meynadier, L., Valet, J.P., Shackleton, J.N., 1995. Relative geomagnetic intensity during the last 4 m.y. from the equatorial Pacific. Proc. ODP Sci. Res. 138, 779–795.

Nowaczyk, N.R., Baumann, M., 1992. Combined high resolution magnetostratigraphy and nannofossil biostratigrahy for late quaternary Atlantic Ocean sediments. Deep Sea Res. 39, 567–601.

Nowaczyk, N.R., Frederichs, T.W., Eisenhauer, A., Gard, N., 1994. Magnetostratigraphic data from late quaternary sediments from Yermak Plateau, Arctic Ocean: evidence for four geomagnetic polarity events within the last 170 ka of the Brunhes Chron, Geophys. J. Int. 117, 453–471.

Okuno, M., 2001. Tephrochronology of volcanoes in southern Kyushu (SW Japan) during 30,000 years. In: Programme and Abstracts of The Volcanological Society, Japan, p. 52 (in Japanese).

Ono, K., Matsumoto, I., Miyahisa, M., Teraoka, Y., Kambe, N., 1977. Geology of the Taketa district, with geological sheet map at 1:50,000. Geol. Surv. Jpn. 74–119 (in Japanese with English abstract).

Peate, D.W., Chen, J.H., Wasserbung, G.J., Papanastassiou, D.A., 1996. ^{237}U–^{230}Th dating of a geomagnetic excursion in quaternary basalts of the Albuqurtque Volcanoes Field, New Mexico (USA). Geophys. Res. Lett. 23, 2271–2274.

Perrin, M., Schnepp, E., Shcherbakov, V., 1998. Paleointensity database updated. EOS 79, 198.

Raïs, A., Laj, C., Surmont, J., Gillot, P.Y., Guillou, H., 1996. Geomagnetic field intensity between 70,000 and 130,000 years B.P. from a volcanic sequence on La Réunion, Indian Ocean. Earth Planet. Sci. Lett. 140, 173–189.

Schnepp, E., 1996. Geomagnetic paleointensities derived from volcanic rocks of the Quaternary East Eifel volcanic field, Germany. Phys. Earth Planet. Inter. 94, 23–41.

Shibuya, H., Hirata, T., Honjo, T., 1999. Paleomagnetic direction and intensity of the Aso-2 pyroclastic flow. In: Proceedings of the 1999 Japan Earth and Planetary Science Joint Meeting, Tokyo (Abstracts).

Shirai, M., 2001. The widespread tephras in middle pleistocene found in eastern Japan Sea. Chikyu Monthly 23, 600–604 (in Japanese).

Tauxe, L., Shackleton, N.J., 1994. Relative paleointensity records form the Ontong–Java Plateau. Geophys. J. Int. 117, 769–782.

Thellier, E., Thellier, O., 1959. Sur I'intensite du champ magnetique terrestre dans le passe histrique et geologique. Ann. Geophys. 15, 285–376.

Tric, E., Valet, J.P., Gillot, P.Y., Lemeur, I., 1994. Absolute paleointensities between 60 and 160 kyear B.P. from Mount Enta (Sicily). Phys. Earth Planet. Inter. 85, 113–129.

Weatgate, J., 1988. Isothermal plateau fission-track age of the late pleistocene Old Crow tephra, Alaska. Geophys. Res. Lett. 15, 376–379.

Yamazaki, T., Ioka, N., 1994. Long-term secular variation of the geomagnetic field during the last 200 kyr recorded in sediment cores from the western equatorial Pacific. Earth Planet. Sci. Lett. 128, 527–544.

York, D., 1966. Least-squares fitting of a straight line. Can. J. Phys. 44, 1079–1086.

York, D., 1968. The best isochron. Earth Planet. Sci. Lett. 2, 479–482.

Yoshikawa, S., Kuwae, M., 2001. High resolution tephrochronology for the past 400 ky obtained from Lake Biwa sediments. Chikyu Monthly 23, 594–599 (in Japanese).